

1 **Assessing the Ducting Phenomenon and its Potential Impact on**  
2 **GNSS Radio Occultation Refractivity Retrievals over the**  
3 **Northeast Pacific Ocean using Radiosondes and Global**  
4 **Reanalysis**

5 Thomas E. Winning Jr.<sup>1</sup>, Feiqin Xie<sup>1</sup> and Kevin J. Nelson<sup>1,a</sup>  
6 <sup>1</sup>Texas A&M University – Corpus Christi, Corpus Christi, 78412, USA  
7 <sup>a</sup>now at: Jet Propulsion Laboratory, California Institute of Technology, Pasadena, 91109, USA  
8 *Correspondence to:* Thomas E. Winning Jr. (twinning@islander.tamucc.edu)  
9

10 **Abstract.** In this study, high-resolution radiosondes from the MAGIC field campaign and ERA5  
11 global reanalysis data are used to assess the elevated ducting layer characteristics along the transect  
12 over the northeastern Pacific Ocean from Los Angeles, California to Honolulu, Hawaii. The  
13 planetary boundary layer (PBL) height (PBLH) increases as the strength of the refractivity gradient  
14 decreases westward along the transect. The thickness of the prevailing ducting layer remains  
15 remarkably consistent (~110 m) in the radiosonde data. On the other hand, the ERA5 generally  
16 resolves the ducting features well, but underestimates the ducting height and strength especially  
17 over the trade cumulus region near Hawaii. A simple two-step end-to-end simulation is used to  
18 evaluate the impact of the elevated ducting layer on RO refractivity retrievals. A systematic  
19 negative refractivity bias (*N*-bias) below the ducting layer is observed throughout the transect,  
20 peaking (−5.42%) approximately 80 meters below the PBLH, and gradually decreasing towards  
21 the surface (−0.5%). The *N*-bias shows strong positive correlation with the ducting strength. The  
22 ERA5 data underestimate the *N*-bias with the magnitude of the underestimation increasing  
23 westward along the transect.

24  
25  
26  
27  
28  
29

## 30 **1 Introduction**

31 The troposphere, where most weather occurs, consists of two main layers: the planetary boundary  
32 layer (PBL) and the free atmosphere (FA) (Garratt, 1994). The PBL characteristics change  
33 frequently on both spatial and temporal scales and the PBL height (PBLH) can impact the  
34 exchange of heat, momentum, and particulate matter with the FA, making it a critical factor in  
35 global energy balances and water cycling (Stull 1988; Ramanathan et al. 1989; Klein and  
36 Hartmann 1993). Regular PBL observations are mainly limited to in situ measurements from  
37 surface stations and radiosondes. However, spatially and temporally dense in situ PBL  
38 observations are typically only available from field campaigns such as the Boundary Layer  
39 Experiment 1996 (BLX96, Stull et al. 1997), the Variability of the American Monsoon Systems  
40 (VAMOS) Ocean-Cloud-Atmosphere-Land Study Regional Experiment (VOCALS-REx, Wood  
41 et al. 2011), and the Marine Atmospheric Radiation Measurement (ARM) Global Energy and  
42 Water Experiment (GEWEX) Cloud System Studies (GCSS) Pacific Cross Section  
43 Intercomparison (GPCI) Investigation of Clouds (MAGIC, Zhou et al. 2015). Satellite  
44 observations of the PBL are also limited due to signal attenuation of the conventional infrared  
45 sounder in the lower troposphere and the low vertical resolution of microwave sounding  
46 instruments. Additionally, while the depth of the PBLH can vary from a couple hundred meters to  
47 a few kilometers (Ao et al. 2012; von Engel'n and Teixeira 2013), the transition layer from the PBL  
48 to the FA is typically on the order of tens to hundreds of meters thick (Maddy and Barnet 2008),  
49 rendering ineffective PBL sensing from the low vertical resolution passive infrared and microwave  
50 sounders.

51 On the other hand, Global Navigation Satellite System (GNSS) radio occultation (RO) provides  
52 global atmospheric soundings with a vertical resolution of approximately 100 m in the lower  
53 troposphere under all weather conditions (Kursinski et al., 1997, 2000; Gorbunov et al., 2004).  
54 One of the major GNSS RO missions is the Formosat-3/Constellation Observing System for  
55 Meteorology, Ionosphere, and Climate (COSMIC), later referred to as COSMIC-1 (Anthes et al.  
56 2008), and its follow-on mission COSMIC-2 (Schreiner et al. 2020). Numerous studies have  
57 documented the high value of GNSS RO for profiling the PBL and determining the PBLH (Ao et  
58 al. 2008; Xie et al. 2008; Basha and Ratnam 2009; Guo et al. 2011; Ao et al. 2012; Ho et al. 2015;  
59 Winning et al. 2017; Nelson et al. 2021).

60 The advancement of the GNSS RO technique with open-loop tracking (Ao et al., 2003; Beyerle et  
61 al., 2003; Sokolovskiy et al., 2006) along with the implementation of radio-holographic retrieval  
62 algorithms (Gorbunov, 2002; Jensen et al., 2003; Jensen et al., 2004) have led to much improved  
63 PBL sounding quality. However, probing the marine PBL remains challenging as systematic  
64 negative biases are frequently seen in RO refractivity retrievals (Xie et al. 2010; Feng et al. 2020).  
65 One major cause of the refractivity bias (hereafter *N*-bias) is the RO retrieval error due to elevated  
66 atmospheric ducting often seen near the PBLH (Sokolovskiy 2003; Ao et al. 2003; Xie et al., 2006;  
67 Ao et al., 2007). This elevated ducting prevails over the subtropical eastern oceans (von Englen et  
68 al., 2003; Lopez, 2009; Feng et al., 2020), and the horizontal extent of ducting in these regions can  
69 be on the order of thousands of kilometers (Xie et al. 2010; Winning et al. 2017). In the presence  
70 of ducting, the vertical refractivity gradient exceeds the critical refraction threshold for L-band  
71 frequencies (i.e.,  $dN/dz \leq -157$  N-units  $\text{km}^{-1}$ ). The steep negative refractivity gradient is often  
72 observed in the vicinity of the PBLH, which is typically caused by an atmospheric temperature  
73 inversion, a sharp decrease in moisture, or a combination of both. When ducting is present, the  
74 Abel inversion (e.g., Fjeldbo et al., 1971) in the standard RO retrieval process encounters a non-  
75 unique inversion problem due to a singularity in the bending angle, resulting in large, systematic  
76 underestimation of refractivity (*N*) below the ducting layer (Ao et al., 2003; Sokolovskiy, 2003;  
77 Xie et al. 2006). The large uncertainty in RO refractivity coupled with the singularity in bending  
78 angle hinders assimilation of RO observations into numerical weather models, resulting in  
79 discarding of a significant percentage of RO measurements inside the PBL (Healy, 2001).

80 To comprehensively assess the potential impact of ducting on GNSS RO retrievals, we begin by  
81 constructing a detailed ground truth of PBL ducting statistics. This is derived from an extensive  
82 set of high-resolution radiosonde data over the northeastern Pacific Ocean, a region known for  
83 prevailing ducting conditions. Subsequently, we conduct a simulation study using the radiosonde  
84 data to evaluate the *N*-biases caused by varying ducting characteristics. Section 2 provides details  
85 of the two data sets used for this study: high-resolution radiosondes over the northeastern Pacific  
86 Ocean and the colocated ECMWF Reanalysis version 5 (ERA5, Hersbach et al. 2020) profiles.  
87 Additionally, we discuss the collocation criteria and the detection method for ducting layer and the  
88 corresponding PBLH. Section 3 presents the ducting statistics for key variables, such as ducting  
89 height, PBLH, minimum refractivity gradient, and sharpness parameter. The characteristics of  
90 ducting including the thickness and strength along the cross-section are also shown. Furthermore,

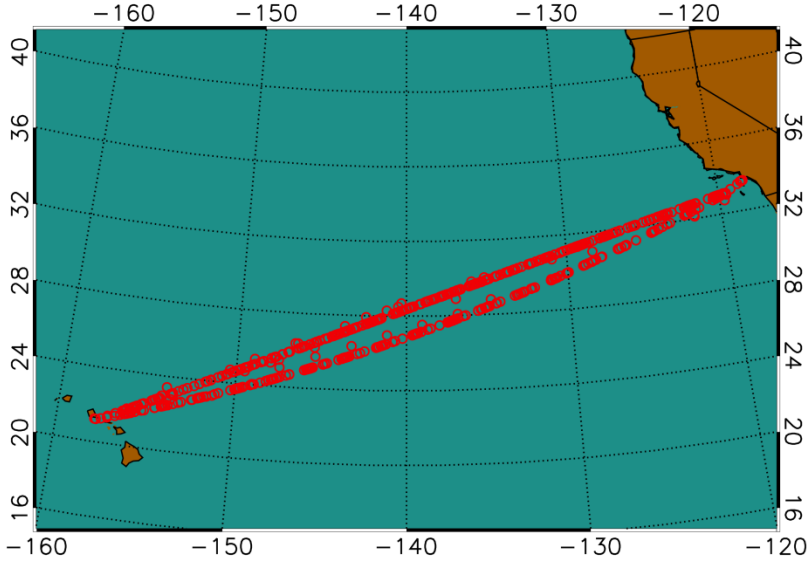
91 we evaluate the ducting-induced  $N$ -bias in GNSS RO refractivity retrievals by carrying out a two-  
92 step end-to-end simulation. Section 4 summarizes the findings and discusses the direction of future  
93 research.

## 94 **2 Data and methods**

### 95 **2.1 MAGIC radiosonde and colocated ERA5 data**

96 A collection of high-resolution radiosondes from the Marine Atmospheric Radiation Measurement  
97 (ARM) GCSS Pacific Cross Section Intercomparison (GPCI) Investigation of Clouds (MAGIC)  
98 are utilized as the primary data set in this analysis (Zhou et al. 2015; Lewis 2016). The MAGIC  
99 field campaign took place from 26 September 2012 to 2 October 2013 as part of the U.S  
100 Department of Energy ARM Program Mobile Facility 2 (AMF2) aboard the Horizon Lines  
101 container ship, *Spirit*, which completed 20 round trip passes between Los Angeles, California and  
102 Honolulu, Hawaii during the yearlong data collection period (Painemal et al., 2015; Zhou, 2015).  
103 During each transit, radiosondes were launched at 6-hour intervals from the beginning of the  
104 program through the end of June 2013; the observation frequency increased to every 3 hours from  
105 July 2013 through the end of the campaign (Zhou et al., 2015). A total of 583 MAGIC radiosonde  
106 profiles were collected during the field campaign (Zhou et al., 2015), all with a vertical sampling  
107 frequency of 0.5 Hz (2 seconds), which provides an average vertical resolution of ~8 m below 3  
108 km, but varies due to local vertical motion.

109 Use of this data set serves multiple benefits. First, the northeast Pacific transitions from a shallow  
110 stratocumulus-topped PBL to a higher, trade-cumulus boundary layer regime along the GPCI  
111 transect (Garratt, 1994). Second, the large number of observations over a 12-month time frame  
112 provides high temporal (diurnal and seasonal) and spatial profiling of the PBL along the GPCI  
113 transect seen in Fig.1. Finally, ducting is prevalent throughout the domain over which the  
114 observations were captured creating an opportunity to perform an analysis over a natural cross-  
115 section of X (zonal) and Z (vertical) dimensions.



116  
117 **Figure 1: Location of radiosonde observations from the MAGIC field campaign October 2012–September 2013.**  
118

119 The radiosonde profiles are colocated with ERA5 model profiles. The ERA5 data have a horizontal  
120 grid resolution of  $0.25^\circ \times 0.25^\circ$ , 1-hour temporal resolution, and 137 non-linear vertical model levels  
121 from the surface to 0.01 hPa. The model level density decreases with height: on average, there are  
122 19 model levels below 1 km (10 –100 m resolution), which reduces to 8 levels between 1 and 2  
123 km (100 – 160 m resolution), and further reduces to 5 levels between 2 and 3 km (160-200 m  
124 resolution). Each MAGIC radiosonde profile was colocated with the nearest ERA5 grid point that  
125 is within 1.5 hours of the closest 3-hourly model profile.

## 126 **2.2 PBLH detection with the minimum gradient method**

127 At GNSS L-band frequencies, the atmospheric refractivity ( $N$  in N-units) is derived from the  
128 refractive index  $n$ , where  $N = (n - 1) \times 10^6$  and, in the neutral atmosphere (Kursinski et al., 1997),  
129 is a function of the atmospheric pressure ( $P$  in mb), temperature ( $T$  in K), and partial pressure of  
130 water vapor ( $P_w$  in mb) as seen in Eq. (1) from Smith and Weintraub (1953).

$$131 \quad N = 77.6 \frac{P}{T} + 3.73 \times 10^5 \frac{P_w}{T^2}, \quad (1)$$

132 Over the subtropical eastern oceans, a sharp decrease in moisture is often associated with a strong  
133 temperature inversion marking a clear transition from the PBL to the FA. Both the distinct decrease  
134 in moisture and the temperature inversion lead to a sharp negative refractivity gradient which can  
135 be precisely detected from GNSS RO. Numerous studies have implemented the simple gradient

136 method to detect the PBLH, i.e., the height of the minimum refractivity gradient (Xie et al., 2006;  
137 Seidel et al., 2010; Ao et al., 2012).

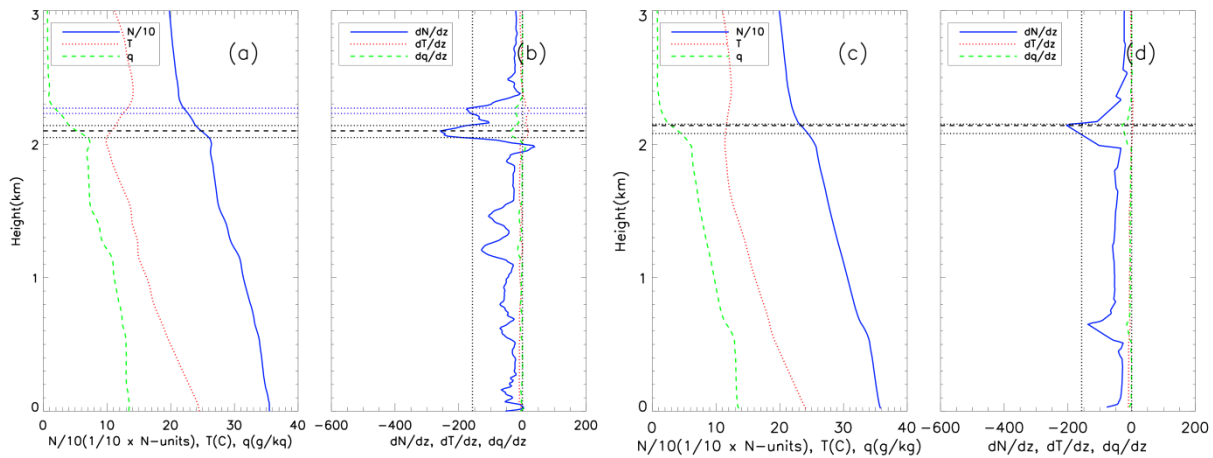
138 In this study, the MAGIC radiosonde refractivity profiles were first interpolated to a uniform 10  
139 m vertical grid and then smoothed by a 100 m boxcar window to reduce the noise in the gradient  
140 profile resulting from the high sampling rate. Moreover, the 100 m smoothed radiosonde will be  
141 more consistent with the vertical resolution of GNSS RO measurements (e.g. Gorbunov et al.,  
142 2004). Colocated ERA5 data were also vertically interpolated to the same 10 m grid but not  
143 smoothed as these data do not contain the inherent noise as the radiosonde observations. In the  
144 case of both data sets, quadratic interpolation is used to translate the refractivity profiles from their  
145 native height values to a uniform height. Finally, as the elevated ducting layer is the focus of this  
146 study, the lowest 0.3 km above mean-sea-level of the  $N$ -profile are excluded (e.g., Xie et al., 2012).  
147 Subsequently, the height of the minimum refractivity gradient (within 0.3 km and 5 km) will be  
148 identified as the PBLH.

### 149 **2.3 Ducting layers**

150 The refractivity gradient profile is calculated by differentiating the 10 m interpolated refractivity  
151 profile with respect to height. When the vertical refractivity gradient is less than the critical  
152 refraction ( $dN/dz < -157.0$  N-units  $\text{km}^{-1}$ ), ducting occurs (Sokolovskiy, 2003). A ducting layer is  
153 identified as any interval of continuous points with a vertical refractivity gradient equal to or less  
154 than  $-157$  N-units  $\text{km}^{-1}$ . Instances of multiple ducting layers occurring within a profile are present  
155 for both the MAGIC (31.5%) and ERA5 (6.7%) data sets. In this study, we only recognize one  
156 dominant “ducting layer” in each profile where the minimum vertical gradient is located. The  
157 ducting layer thickness ( $\Delta h$ ) is defined as the interval between the top and bottom of the ducting  
158 layer where the refractivity gradients reach critical refraction. Similarly, the strength of each  
159 ducting layer ( $\Delta N$ ) is defined as the refractivity difference between the bottom and top of the  
160 ducting layer. The ducting layer height is defined as the height of the top of the ducting layer (Ao,  
161 2007), which is slightly above the PBLH.

162 Figure 2 shows vertical profiles of refractivity ( $N$ -units/10), temperature ( $T$ ), and specific humidity  
163 ( $q$ ) along with their respective vertical gradients ( $dN/dz$ ,  $dT/dz$ , and  $dq/dz$ ) from a representative  
164 MAGIC radiosonde (Fig. 2a,b) case located at ( $23.69^\circ$ ,  $-150.02^\circ$ ), and its colocated ERA5 (Fig.  
165 2c,d) profile at ( $23.75^\circ$ ,  $-150.00^\circ$ ). The PBLH of the radiosonde (2.10 km) is almost identical to

166 the colocated ERA5 (2.14 km) and the “dominant” ducting layer near the PBLH demonstrates  
 167 similar thickness. However, a second, weaker ducting layer seen in the radiosonde above the PBLH  
 168 was not captured by the ERA5. Note that the weak gradients seen above the minimum in the ERA5  
 169 refractivity gradient (Fig. 2d) are a result of the vertical derivative being calculated from the  
 170 interpolated ERA5 refractivity profile and do not appear for larger interpolation intervals  
 171 suggesting that the non-linearity of the ERA5 vertical grid at this height affects the vertical  
 172 gradient. These features of approximately 15 N-units km<sup>-1</sup> magnitude are only noticed in the  
 173 plotting and do not impact the results of the study, as only the moisture-induced minimum gradient  
 174 values are large enough in magnitude to exceed the minimum gradient threshold.



175  
 176 **Figure 2: Vertical profiles of refractivity ( $N$ -units /10, solid blue), temperature ( $T$  in  $^{\circ}\text{C}$ , dotted red) and specific humidity**  
 177 **( $q$  in  $\text{g kg}^{-1}$ , dashed green) for (a) radiosonde at (23.69 $^{\circ}$ , -150.02 $^{\circ}$ ) launched at 2012-10-02, 05:30 UTC, and (c) colocated**  
 178 **ERA5 at (23.75 $^{\circ}$ , -150.00 $^{\circ}$ ); and associated gradient profiles for radiosonde (b) and ERA5 (d). The horizontal dashed line**  
 179 **highlights the height of the minimum gradient, i.e., PBLH. The paired horizontal dotted lines represent the bottom and top**  
 180 **of the two ducting layers in the radiosonde profile (a and b) but only one in the ERA5 profile (c and d).**

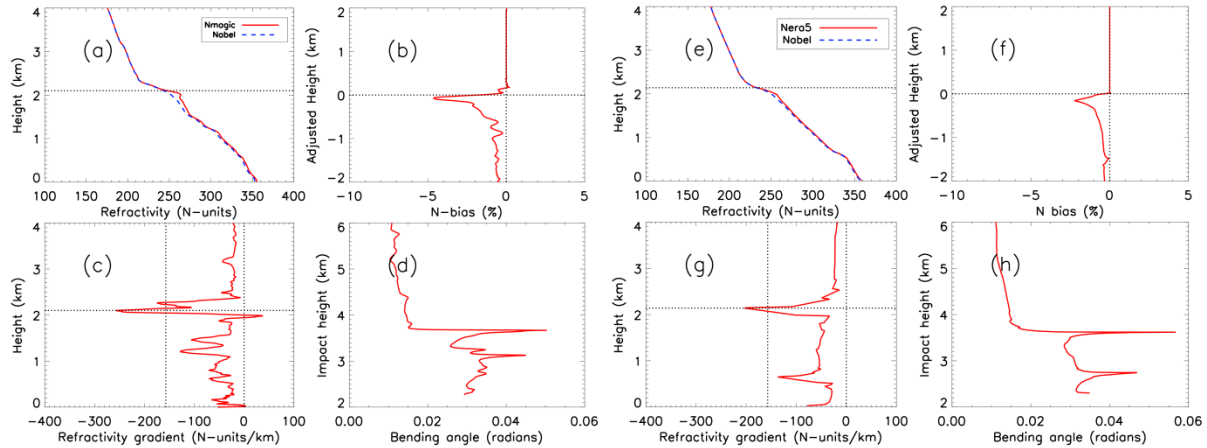
## 181 2.4 Evaluation of GNSS RO $N$ -bias resulting from ducting

182 In order to estimate the systematic negative  $N$ -bias in GNSS RO observations in the presence of  
 183 ducting, we use an end-to-end simulation on the radiosonde and ERA5 refractivity profiles. The  
 184 simulation consists of a two-step process adapted from Xie et al. (2006). The first step is to  
 185 simulate the 1-dimensional GNSS RO bending angle as a function of impact parameter (i.e., the  
 186 product of refractive index and the radius of the Earth’s curvature) by forward Abel integration of  
 187 an input refractivity profile assuming a spherically symmetric atmosphere (Fjeldbo and Eshleman,  
 188 1968; Eshleman, 1973; Sokolovskiy, 2001). The second step is to simulate the GNSS RO  
 189 refractivity retrieval by applying the Abel inversion on the simulated bending angle from step one.  
 190 In the absence of ducting, the impact parameter increases monotonically with height, allowing a

191 unique solution to the inverse Abel retrieval that is the same as the original refractivity profile  
192 input. However, in the presence of an elevated ducting layer, the Abel retrieval systematically  
193 underestimates the refractivity profile due to the non-unique Abel inversion problem resulting  
194 from the singularity in bending angle across the ducting layer (Sokolovskiy 2003; Xie et al., 2006).  
195 It should be noted that after the 100 m vertical smoothing on radiosonde (no smoothing on ERA5)  
196 profiles as described in section 2.2, an additional 50 m vertical smoothing has been applied to the  
197 simulated bending angle profiles of both radiosonde and ERA5 data sets to alleviate the challenge  
198 of integration through the very sharp bending angle resulting from ducting in the inverse Abel  
199 integration procedure (Feng et al., 2020).

200 Figure 3 shows the end-to-end simulation results for the same radiosonde (a–d) and the colocated  
201 ERA5 (e–h) cases from Fig. 2. Figures 3a and 3e show refractivity profiles from the radiosonde  
202 ( $N_{MAGIC}$ ) and the colocated ERA5 ( $N_{ERA5}$ ) data as well as their corresponding Abel refractivity  
203 retrievals ( $N_{Abel}$ ). The refractivity gradients are shown in Figures 3c and 3g. The derived PBLH is  
204 marked by a horizontal dotted line. The peak bending angles in Figures 3d and 3h are consistent  
205 with the sharp refractivity gradient. Figure 3b shows the fractional  $N$ -bias between the simulated  
206 Abel retrieved RO refractivity profile and the radiosonde, whereas Figure 3f shows the same for  
207 the ERA5 profile. Considering the significant spatial and temporal variations of ducting height  
208 along the transect, each  $N$ -bias profile is displayed as a function of an adjusted height, which is the  
209 height minus the corresponding PBLH for the purposes of profile intercomparison. For example,  
210 the zero-adjusted height refers to the PBLH for each individual profile. The systematic negative  
211  $N$ -bias is shown below the ducting layer marked by the PBLH in both cases, with the biases  
212 decreasing at lower altitude, the largest magnitude bias ( $-5\%$  for radiosonde;  $-2.5\%$  for ERA5)  
213 close to the ducting height and a minimum magnitude approaching zero near the surface.





214  
 215 **Figure 3: End-to-end simulation results for MAGIC radiosonde launched at 0530 UTC on 20121002 showing: (a)  $N_{MAGIC}$**   
 216 **(solid red) and  $N_{Abel}$  (blue dashed) from surface to 4 km; (b) PBLH adjusted  $N$ -bias; (c) refractivity gradient and (d) bending**  
 217 **angle vs. impact parameter. Panels e-h show end-to-end simulation results for the colocated ERA5 profile.**

218 **3 Analysis**

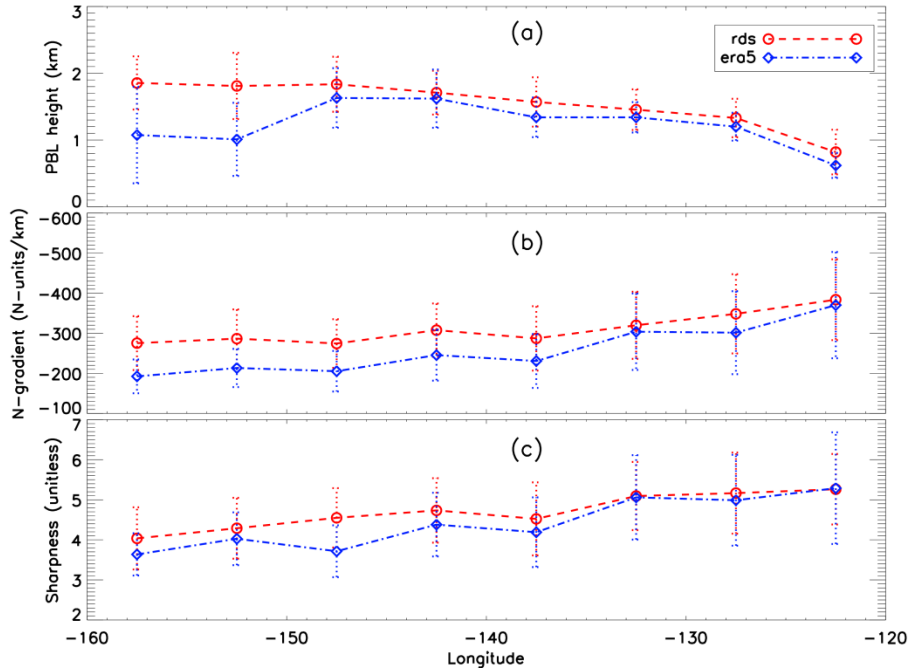
219 Quality control for radiosonde (and colocated ERA5) profiles was based on five key criteria. First,  
 220 a total of 19 radiosonde and 24 ERA5 profiles near the southern California coast were removed  
 221 due to their positions east of  $-120^\circ$  or anomalously high PBL (PBLH  $> 3.0$  km) with no distinct  
 222 minimum gradient. The remaining profiles in the easternmost portion of the domain were too few  
 223 in number to calculate meaningful statistics. Second, any profile lacking critical refraction (i.e.  
 224  $dN/dz < -157$  N-units  $\text{km}^{-1}$ ) points was excluded from the analysis which resulted in the removal  
 225 of 47 radiosonde and 176 ERA5 profiles. Third, the noisy bending angle could result in errors in  
 226 Abel refractivity retrieval and cause positive  $N$ -bias. Therefore, the profiles with  $N$ -bias greater  
 227 than  $+0.5\%$  are excluded resulting in the removal of 61 MAGIC profiles and 16 ERA5 profiles.  
 228 Fourth, the profiles with only surface ducting, i.e., below 300 m threshold, are discarded. Finally,  
 229 25 radiosonde profiles and 2 ERA5 profiles were removed due to the Abel retrieval failure. After  
 230 implementing all quality control measures, the number of radiosonde and ERA5 profiles used for  
 231 the  $N$ -bias analysis is reduced to 396 and 319 profiles, respectively.

232 **3.1 PBL analysis**

233 To evaluate the ducting properties along the transect from the coast of southern California to  
 234 Hawaii, we group the MAGIC radiosonde and the colocated ERA5 profiles into eight  $5^\circ$  longitude  
 235 bins between  $-160.0^\circ$  and  $-120.0^\circ$ , which allows for the spatial variation of the PBL, ducting layer

236 and the associated properties along the transect to be easily illustrated. Figure 4 shows the median  
237 value of PBLH (a), minimum gradient (b) and sharpness parameter (c) along the transect. The  
238 median-absolute-deviation (MAD) for each parameter is also shown.

239 In Fig. 4a, the MAGIC radiosondes (rds) clearly show the gradual increase of the PBLH along the  
240 transect from the shallow stratocumulus-topped PBL (~800 m) near the southern California coast  
241 westward to the much deeper trade-cumulus regime (~1.8 km) near Hawaii. A similar structure is  
242 seen in the colocated ERA5 data but with an average low bias of 165 m below the radiosonde.  
243 However, a nearly 800 m underestimation in PBLH over the two westernmost bins near Hawaii is  
244 also seen, this is consistent with what is found over the equivalent trade cumulus region of the  
245 subtropical southeast Pacific Ocean (Xie et al., 2012). Such a discrepancy could be due to the  
246 sensitivity of the gradient method to the vertical resolution of the data. Over the western segment  
247 of the transect (near Hawaii), two major gradient layers (one at ~1 km and the other at ~2 km) with  
248 comparable refractivity gradients are often observed (e.g., Fig. 2). The gradient layer near 2 km is  
249 well-known as the trade-wind inversion (Riehl, 1979; Ao et al., 2012; Xie et al., 2012), while the  
250 lower-level gradient layer at ~1 km, is generally called a mixing layer (Xie et al., 2006). Due to  
251 the differences in vertical sampling noted in Section 2.1, the ERA5 data are more likely to resolve  
252 the sharp gradient structure below 1 km than the one at higher altitude. This could result in  
253 resolving the mixing layer (below 1 km) with the sharpest refractivity gradient, instead of the trade-  
254 wind inversion near 2 km in the ERA5 data. Note that the larger median absolute deviation for the  
255 westernmost bins compared to the rest of the transect illustrates the existence of greater PBLH  
256 variability closer to the trade-cumulus boundary layer regime. The westward decreasing magnitude  
257 of the minimum refractivity gradient (Fig. 4b) and sharpness parameter (Fig. 4c) indicates the  
258 westward weakening of moisture lapse rate and/or temperature inversion across the PBL top,  
259 which is consistent with the decreasing synoptic-scale subsidence from the California coast to  
260 Hawaii (Riehl, 1979).



261  
 262 **Figure 4: Zonal transect of 5° bin MAGIC and ERA5 PBLH (a), minimum refractivity gradient (b) and sharpness**  
 263 **parameter (c) for MAGIC (median in red circle and dashed line, MAD in red dotted error bars) and ERA5 (median in blue**  
 264 **diamond and dot-dashed line, MAD in blue dotted error bars).**  
 265

266 It is also notable that the ERA5 systematically underestimates not only the PBLH but also the  
 267 magnitude of the minimum gradient across the entire transect. This can also be seen in the  
 268 sharpness parameter west of  $-132.5^\circ$ . This discrepancy could be partially attributed to the decrease  
 269 in vertical sampling in ERA5 profiles as compared to the radiosondes, the result of which leads to  
 270 a weaker PBL refractivity gradient and coincides with an increasing PBLH. Therefore, the  
 271 underestimation of the ERA5 minimum refractivity gradient increases in magnitude from east to  
 272 west and becomes most prominent near Hawaii where the PBLH reaches the maximum height  
 273 over the region.

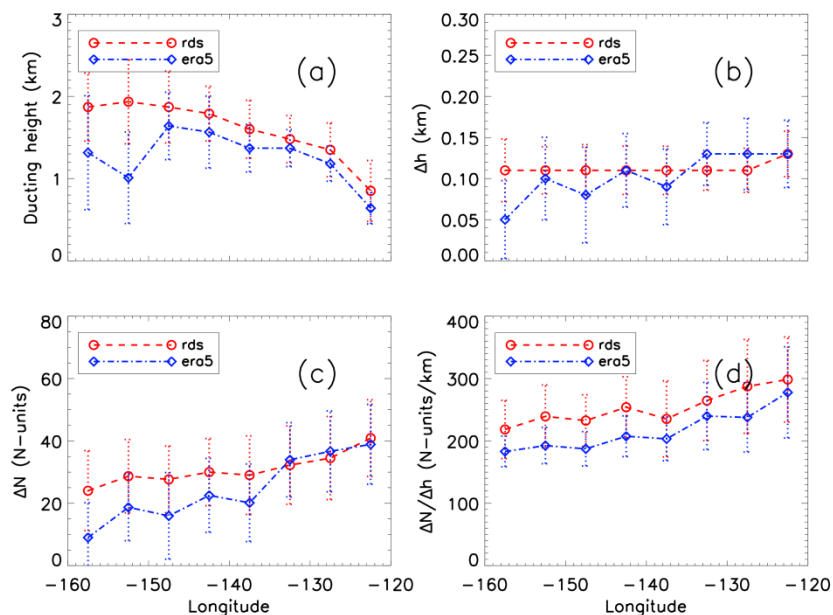
### 274 3.2 Ducting characteristics

275 As introduced in Sect. 2.3, the key characteristics of the ducting layer along the transect will be  
 276 investigated, these include the ducting layer height, thickness ( $\Delta h$ ), and strength ( $\Delta N$ ), as well as  
 277 the average refractivity gradient within the ducting layer ( $\Delta N/\Delta h$ ).

278 The ducting layer heights from both radiosonde and ERA5 show a westward increase along the  
 279 transect, as seen in Fig. 5a. Note again that the ERA5 shows a systematic  $\sim 100\text{--}200$  m low bias  
 280 when compared to the radiosondes between  $-122.5^\circ$  and  $-147.5^\circ$ , with the difference increasing

281 to more than 500 m near Hawaii. The ducting layer thickness is the median height from the bottom  
 282 of the ducting layer to the top and is expressed in km (Fig. 5b). Ducting thickness ( $\Delta h$ ) for MAGIC  
 283 shows a near constant value of 110 m across the entire transect with only a slight increase to 130  
 284 m at  $-122.5^\circ$ , consistent with Ao et al. (2003). Conversely, the ERA5 shows a constant but slightly  
 285 thicker ducting layer to the east of  $-137.5^\circ$  and then a decreasing thickness to the west of  $-137.5^\circ$   
 286 (Fig. 5b).

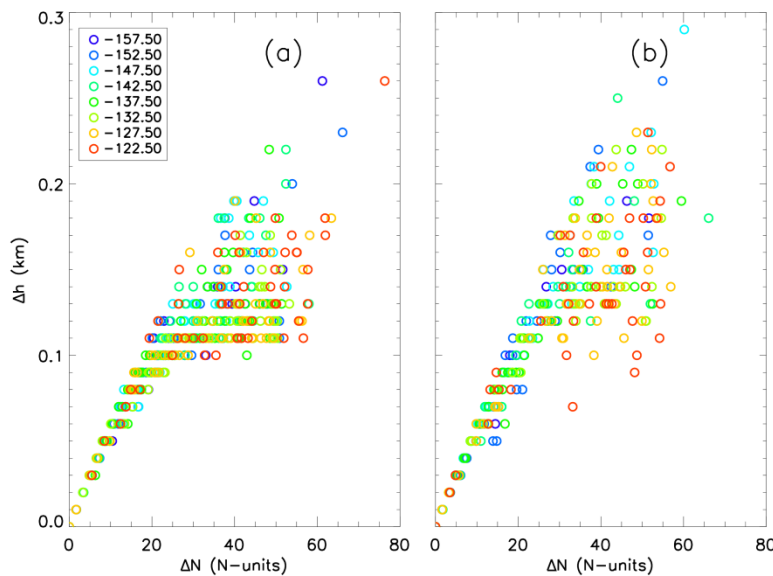
287 The ducting layer strength is the decrease in refractivity from the bottom of the ducting layer to  
 288 the top (Fig. 5c) and the ratio  $\Delta N/\Delta h$  reflects the average gradient of the ducting layer (Fig. 5d).  
 289 The ducting strength ( $\Delta N$ ) for the radiosondes generally ranges from 25 N-units near Hawaii to 40  
 290 N-units near the coast of California. Both  $\Delta N$  and  $\Delta N/\Delta h$  show an overall westward decreasing  
 291 trend along the transect which is consistent with the decrease in magnitude of the refractivity  
 292 gradient (Fig. 4b). Note that MAGIC and ERA5 show similar ducting strength in the eastern part  
 293 of the region but diverge near  $-137.5^\circ$  with ERA5 10 to 20 N-units weaker than the MAGIC  
 294 profiles. On the other hand, ERA5 shows a systematically lower average refractivity gradient  
 295 ( $\Delta N/\Delta h$ ) than MAGIC throughout the transect, indicating the challenge in ERA5 to consistently  
 296 resolve the sharp vertical structure in refractivity, and likewise in temperature and moisture  
 297 profiles, across such a thin ducting layer. The problem becomes acutely clear near the trade  
 298 cumulus region.



299

300 Figure 5: Zonal transect of 5° bin median (a) ducting height, (b) ducting layer thickness ( $\Delta h$ ), (c) ducting layer strength  
 301 ( $\Delta N$ ), and (d) average ducting layer gradient  $\Delta N/\Delta h$  for MAGIC (median in red circle and red-dashed line, MAD in red-  
 302 dotted error bars) and ERA5 (median in blue diamond and dot-dashed line, MAD in blue-dotted error bars).  
 303

304 Figure 6 shows ducting layer thickness as a function of ducting layer strength, with each data point  
 305 colored by its respective longitude bin. The relationship between  $\Delta h$  and  $\Delta N$  is not longitude-  
 306 dependent for either data set, but a linear trend is evident for thinner ducting layers ( $\Delta h < 0.1$  km)  
 307 with weaker ducting strength ( $\Delta N < \sim 25$  N-units). However, for the ducting layers thicker than 0.1  
 308 km, such a trend becomes less identifiable, and the ducting strength  $\Delta N$  begins to show more  
 309 variability toward larger values.  
 310



311 Figure 6: Comparison of individual profiles' ducting strength ( $\Delta N$ ) vs. ducting thickness ( $\Delta h$ ) for MAGIC (a) and ERA5  
 312 (b). The color of each circle represents the location of the 5° longitude bin of each observation.  
 313

### 314 3.3 Ducting-induced GNSS RO $N$ -bias statistics

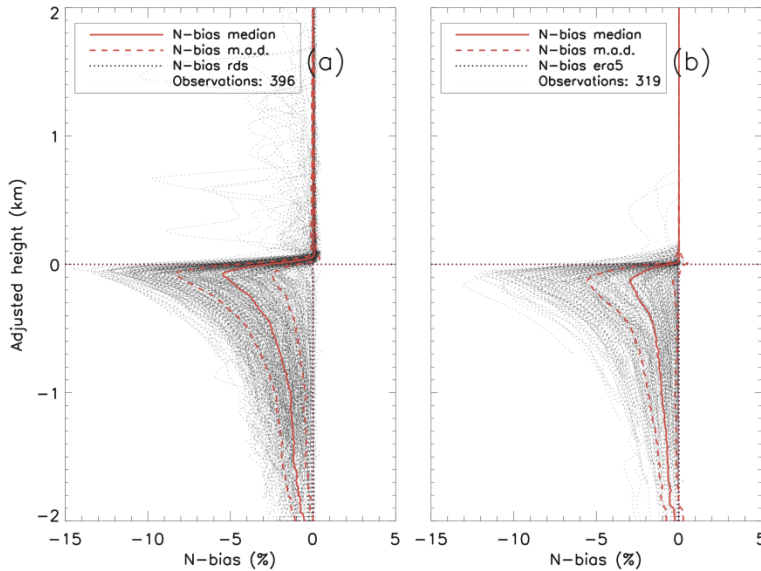
315 To estimate the systematic negative  $N$ -bias in GNSS RO observations due to ducting, we have  
 316 applied the end-to-end simulation described in Sect. 2.4 to all radiosonde and ERA5 refractivity  
 317 profiles with at least one elevated ducting layer detected. The  $N$ -bias along the transect as well as  
 318 its relationship to the ducting properties are presented below.

#### 319 3.3.1 Assessing ducting-induced $N$ -bias

320 Figure 7 shows a composite of both MAGIC (396 profiles) and ERA5 (319 profiles)  $N$ -bias profiles  
 321 which have been displayed as a function of an adjusted height, which is the height minus the

322 derived PBLH, with the median  $N$ -bias and MAD overlaid. The systematic negative  $N$ -bias peaks  
 323 at approximately 100 m below the PBLH and decreases at lower altitude. The peak median value  
 324 of the  $N$ -bias for radiosondes is  $-5.42\%$  (MAD,  $2.92\%$ ), nearly twice the ERA5 value of  $-2.96\%$   
 325 (MAD,  $2.59\%$ ), indicating the significant underestimation of ducting strength in ERA5 data.  
 326 However, the variabilities (MAD) of the radiosonde and ERA5 data are within  $0.33\%$  of each  
 327 other, indicating that ERA5 data successfully capture the variations of ducting features seen in the  
 328 radiosondes. It is worth noting that many radiosonde profiles show small negative  $N$ -biases above  
 329 the PBLH (i.e., zero-adjusted height), which is the result of a secondary ducting layer above the  
 330 major ducting layer near the PBLH. Few ERA5 profiles show the presence of the secondary  
 331 ducting layer above PBLH.

332



333  
 334  
 335  
 336  
 337

**Figure 7: Fractional refractivity difference ( $N$ -bias in %) between the simulated Abel-retrieved refractivity profile and the original observation profile, for all individual observations (dotted gray): (a) MAGIC radiosondes (396 total profiles) and (b) ERA5 (319 total profiles) with population median (solid red)  $\pm$  MAD (dashed red). Note the zero value in the adjusted height refers to the PBLH for each individual  $N$ -bias profile.**

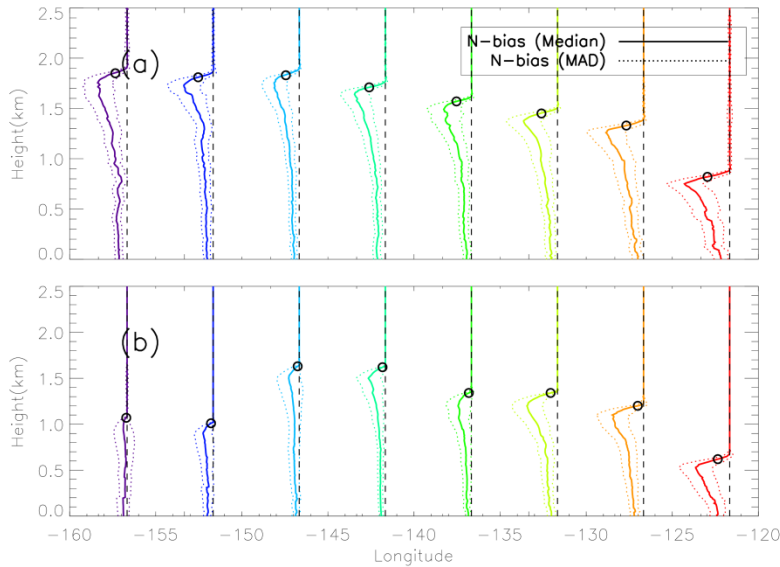
### 338 3.3.2 Zonal variation of the $N$ -bias along the transect

339 To illustrate the large variation in the  $N$ -bias vertical structure resulting from the spatial variations  
 340 of ducting height and strength, Fig. 8 presents the  $N$ -bias profiles (median  $\pm$  MAD) for each  $5^\circ$  bin,  
 341 replacing the zero adjusted height with the median PBLH for each bin. The radiosonde composite  
 342 (Fig. 8a) illustrates the westward transition of the median  $N$ -bias profiles from the largest peak  $N$ -  
 343 bias at  $\sim 0.8$  km near the coast of Los Angeles, California, to a much reduced peak  $N$ -bias but

344 higher altitude of  $\sim 1.8$  km at Honolulu, Hawaii. Table 1 lists detailed statistics of the peak  $N$ -bias  
 345 values at each bin for both radiosonde and ERA5 data. Although the vertical structure of the  $N$ -  
 346 bias profiles along the transect are consistent as seen in Fig. 7, significant changes of the  $N$ -bias  
 347 magnitude and its peak height along the transect are seen.

348 The maximum peak  $N$ -bias ( $-7.86\%$ ) in the radiosonde data is located at the easternmost of the  
 349 transect near California ( $-122.5^\circ$ ), whereas the minimum peak  $N$ -bias ( $-4.37\%$ ) is located near the  
 350 center of the transect ( $-147.5^\circ$ ). Similarly, the ERA5 also show the maximum peak  $N$ -bias  
 351 ( $-5.92\%$ ) near California ( $-122.5^\circ$ ). However, the minimum peak  $N$ -bias ( $-0.77\%$ ) is found near  
 352 Hawaii ( $-157.5^\circ$ ). Overall, the  $N$ -bias values for the ERA5 data set are less than the  $N$ -bias values  
 353 calculated from the radiosonde data set for each longitude bin. However, a noticeable difference  
 354 exists between the ERA5 and radiosonde profiles for the two westernmost longitude bins ( $-157.5^\circ$   
 355 and  $-152.5^\circ$ ) where the ERA5 reveals a much lower and weaker  $N$ -bias than the MAGIC data.

356 The PBLH is above the height of the peak  $N$ -bias for both data sets. The MAGIC data shows a  
 357 maximum difference of 100 m ( $-137.5^\circ$ ) and a minimum difference of  $\sim 15$  m ( $-152.5^\circ$ ) while the  
 358 ERA5 PBLH shows greater values for maximum difference (230 m at  $-142.5^\circ$ ) and minimum of  
 359 (45 m at  $-157.5^\circ$ ).



360  
 361 **Figure 8: Median  $N$ -bias (solid)  $\pm$  MAD (dotted) along the north Pacific transect for MAGIC radiosondes (a) and ERA5**  
 362 **(b). Open circles represent the median PBLH for each  $5^\circ$  bin.**

363  
 364 **Table 1: Median and MAD peak  $N$ -bias (%) values for MAGIC radiosondes (RDS) and ERA5 for each  $5^\circ$  bin.**

Peak N-bias (%)				
Longitude	RDS median	RDS MAD	ERA5 median	ERA5 MAD
-157.5°	-5.12	±2.61	-0.77	±1.73
-152.5°	-5.10	±2.97	-1.76	±1.61
-147.5°	-4.37	±2.14	-1.83	±2.10
-142.5°	-5.36	±2.53	-2.95	±2.17
-137.5°	-4.82	±2.96	-2.31	±2.14
-132.5°	-5.90	±3.03	-5.31	±2.68
-127.5°	-6.55	±3.40	-5.45	±2.88
-122.5°	-7.86	±3.15	-5.92	±3.04

365  
366

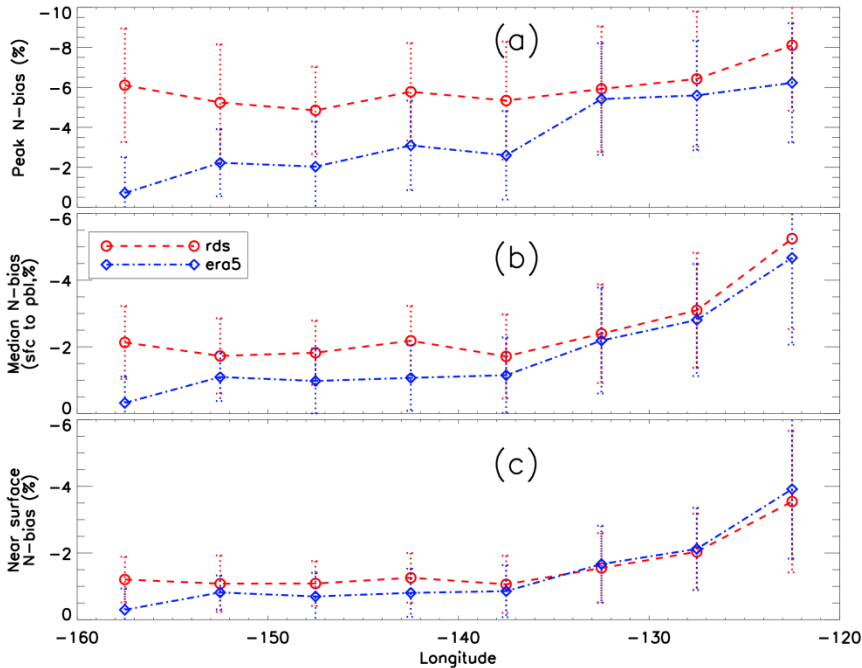
367 Figure 9 further illustrates the peak  $N$ -bias, median PBL  $N$ -bias (0.3 km to PBLH), and the near  
368 surface  $N$ -bias (at 0.3 km) at each bin along the transect. Note the median PBL  $N$ -bias refer to the  
369 median value from the near surface (0.3 km) to the PBLH. Contrary to the general trend of  
370 westward decrease in magnitude of the minimum refractivity gradient (Fig. 4b) and ducting  
371 strength (Fig. 5c), the radiosonde peak  $N$ -bias shows the maximum (median: -8.10%, MAD:  
372 3.26%) near California (-122.5°) and the minimum (median: -4.85%, MAD: 2.18%) over the  
373 transition region (-147.5°) as well as a slight increase to a secondary maximum (median: -6.11%,  
374 MAD: 2.85%) near Hawaii (-157.5°). The median PBL  $N$ -bias and the near surface  $N$ -bias also  
375 show a similar pattern. However, the median  $N$ -bias demonstrates a sharp decrease in the eastern  
376 half of the domain from -5.25% (MAD: 2.71%) at -122.5° to -1.71% (MAD: 1.26%) at -137.5°,  
377 and then remains relatively constant over the western half of the domain. Similarly, the near  
378 surface  $N$ -bias reaches a maximum magnitude of -3.54% (MAD: 2.11%), sharply decreases to  
379 -1.06% (MAD: 0.85%) at -137.5°, and then remains relatively constant over the western half of  
380 the domain.

381 Note that normalizing each  $N$ -bias profile to the PBLH preserves the magnitude of the  $N$ -bias with  
382 various heights. Therefore, the relatively large normalized  $N$ -bias observed near Hawaii indicates  
383 more persistent ducting over the trade-cumulus boundary layer regime compared to the transition  
384 region in the middle of the transect at -147.5° (Fig. 8a).

385 On the other hand, the ERA5 data show a westward decrease of all three  $N$ -biases, systematically  
386 underestimating all three as compared to the radiosondes. This is expected as the decrease of ERA5  
387 vertical resolution at higher altitude leads to a weaker PBL  $N$ -gradient observation (Fig. 4b), and  
388 thus weaker ducting and a smaller ducting-induced  $N$ -bias. Such underestimation of the  $N$ -bias in  
389 the ERA5 minimizes near California where the PBLH is lowest but becomes more severe



390 westward with an increase in height, reaching a maximum magnitude  $N$ -bias difference near  
 391 Hawaii. In this case, the peak  $N$ -bias is merely  $-0.71\%$  (MAD:  $1.80\%$ ) as compared to  $-6.23\%$   
 392 (MAD:  $2.98\%$ ) at  $-122.5^\circ$  (Fig. 9a). The large difference seen in the  $N$ -bias along the transect  
 393 strongly indicates the challenges of the ERA5 data to resolve the sharp gradient across the ducting  
 394 layer, resulting in a large variation in PBLH of the ERA5 data in the western segment of the region.  
 395 The increasing difference between the radiosonde and ERA5 data from east to west is most  
 396 pronounced in the peak  $N$ -bias cross-section (Fig. 9a) but is also evident in both the median  $N$ -bias  
 397 (Fig. 9b) as well as the near surface  $N$ -bias (Fig. 9c).



398  
 399 **Figure 9: Zonal transect of  $5^\circ$  bin (a) peak  $N$ -bias, (b) median PBL  $N$ -bias (0.3 km to PBLH), and (c) near surface  $N$ -bias at**  
 400 **0.3 km for MAGIC (median in red circle and red-dashed line, MAD in red-dotted error bar) and ERA5 (median in red**  
 401 **blue diamond and dot-dashed line, MAD in blue-dotted error bar)**

402 **4 Summary and Conclusions**

403 In this study, radiosonde profiles from the MAGIC field campaign have been analyzed to  
 404 investigate ducting characteristics and the induced systematic refractivity biases in GNSS RO  
 405 retrievals over the Northeastern Pacific Ocean between Hawaii and California. Colocated ERA5  
 406 model reanalysis data were used as a secondary comparison to the radiosonde observations.  
 407 The nearly 1-year high-resolution MAGIC radiosonde data set reveals the frequent presence of  
 408 ducting marked by a sharp refractivity gradient resulting from the large moisture lapse rate across  
 409 a strong temperature inversion layer. The PBLH increases by more than 1 km along the transect

410 from California to Hawaii while the magnitude of the refractivity gradient decreases by 100 N-  
411 units  $\text{km}^{-1}$ . The zonal gradient of both variables illustrates the transition of the PBL from shallow  
412 stratocumulus adjacent to the California coast to deeper trade-wind cumulus that are prevalent near  
413 the Hawaiian Islands.

414 End-to-end simulation on all radiosonde and ERA5 refractivity profiles has been conducted to  
415 estimate the systematic negative  $N$ -bias in GNSS RO observations. The ducting layer maintains  
416 remarkably consistent thickness ( $\sim 110$  m) along the transect with westward decreasing strength  
417 and increasing height. The ERA5 slightly underestimates both the height and strength of the  
418 ducting layer as well as the PBLH. A systematic negative  $N$ -bias below the ducting layer is  
419 observed throughout the transect, peaking ( $-5.42\%$ ) approximately 80 meters below the PBLH,  
420 and gradually decreasing towards the surface ( $-0.5\%$ ).

421 MAGIC radiosondes indicate larger values of both ducting strength ( $\Delta N$ ) and thickness ( $\Delta h$ ) than  
422 ERA5 in the western half of the transect. The opposite is true in the eastern portion of the domain,  
423 and is likely associated with the transition of the cloud layer from open-cell cumulus in the west  
424 to stratocumulus and stratus in the east (Wood et al., 2011; Bretherton et al., 2019). ERA5  
425 systematically underestimates the average ducting layer gradient ( $\Delta N/\Delta h$ ) comparing to the  
426 radiosondes. The largest  $N$ -bias is found over the region with strongest ducting and largest  
427 sharpness parameter. It is worth noting that the PBL over the western portion of the transect near  
428 Hawaii frequently shows two major gradient layers (a mixing layer at  $\sim 1$  km and the trade-  
429 inversion at  $\sim 2$  km), with comparable  $N$ -gradients (e.g., Fig. 2). The much lower PBLH seen in  
430 ERA5 in this region is likely due, in part, to the decreasing number of model levels in ERA5 at  
431 higher altitude, which could lead to higher possibility of identifying the lower gradient layer as the  
432 PBLH. However, the impact of the vertical resolution on the performance of gradient method for  
433 PBLH detection has not been performed in this study and warrants more comprehensive study in  
434 the future.

## 435 **5 Data availability**

436 Data for the Marine Atmospheric Radiation Measurement (ARM) GCSS Pacific Cross Section  
437 Intercomparison (GPCI) Investigation of Clouds (MAGIC, Zhou et al., 2015) can be accessed  
438 through the U.S. Department of Energy's Office of Science  
439 <https://www.arm.gov/research/campaigns/amf2012magic>.

440 Data for the ECMWF Reanalysis version 5 (ERA5, Hersbach et al., 2020) can be accessed at  
441 <https://www.ecmwf.int/en/forecasts/dataset/ecmwf-reanalysis-v5>.

## 442 **6 Author contribution**

443 Author Thomas Winning is responsible for all original text and, data analysis and production of  
444 graphics. Author Kevin Nelson contributed by providing updated data processing code, colocation  
445 of ERA5 data with MAGIC observations and first and second round edits. Author Feiqin Xie is  
446 the academic advisor for the primary author and also provided draft edits and paper organization  
447 and writing guidance.

448

## 449 **7 Competing interests**

450 The authors declare no competing interests, see Acknowledgements for current affiliations.

## 451 **8 Acknowledgements**

452 The authors acknowledge funding support of earlier work from NASA grant (NNX15AQ17G).  
453 Authors T. Winning and K. Nelson were also partially supported by research assistantship from  
454 Coastal Marine System Science Program at Texas A&M University – Corpus Christi. The high-  
455 resolution ERA5 reanalysis data were acquired from ECMWF and the Climate Data Service  
456 (CDS). The MAGIC radiosonde data were provided by the Atmospheric Radiation Measurement  
457 program (ARM) Climate Research Facility sponsored by the U.S. Department of Energy (DOE).  
458 Author K. Nelson’s current affiliation: Jet Propulsion Laboratory, California Institute of  
459 Technology, Pasadena, CA, 91109, USA. Author K. Nelson acknowledges this work was done as  
460 a private venture and not in the author’s capacity as an employee of the Jet Propulsion Laboratory,  
461 California Institute of Technology.

## 462 **References**

463 Anthes, R. A., and Coauthors: The COSMIC/FORMOSAT-3 Mission: Early Results, BAMS, 89, 313–334,  
464 doi.org/10.1175/bams-89-3-313, 2008.

465

466 Ao, C. O., Meehan T. K., Hajj, G. A., Mannucci, A. J., and Beyerle, G.: Lower Troposphere Refractivity Bias in GPS  
467 Occultation Retrievals, J. Geophys. Res., 108, 4577, doi:10.1029/2002JD003216, 2003.

468  
469 Ao, C. O.: Effect of Ducting on Radio Occultation Measurements: An Assessment Based on High-resolution  
470 Radiosonde Soundings, *Radio Sci.*, 42, RS2008, doi.org/10.1029/2006RS003485, 2007.  
471  
472 Ao, C. O., Chan, T. K., Iijima, A., Li, J.-L., Mannucci, A. J., Teixeira, J., Tian, B., and Waliser, D. E.: Planetary  
473 Boundary Layer Information from GPS Radio Occultation Measurements, in: Proceedings of the GRAS SAF  
474 Workshop on Applications of GPSRO Measurements, Vol. 5 of, GRAS SAF Workshop on Applications of GPSRO  
475 Measurements, Reading, United Kingdom, ECMWF and EUMETSAT, 123–131,  
476 [https://www.ecmwf.int/sites/default/files/elibrary/2008/7459-planetary-boundary-layer-information-gps-radio-](https://www.ecmwf.int/sites/default/files/elibrary/2008/7459-planetary-boundary-layer-information-gps-radio-occultation-measurements.pdf)  
477 [occultation-measurements.pdf](https://www.ecmwf.int/sites/default/files/elibrary/2008/7459-planetary-boundary-layer-information-gps-radio-occultation-measurements.pdf), 16–18 June, 2008.  
478  
479 Ao, C. O., Waliser, D. E., Chan, S. K., Li, J.-L., Tian, B., Xie, F., and Mannucci, A. J.: Planetary boundary layer  
480 heights from GPS radio occultation refractivity and humidity profiles, *J. Geophys. Res.*, 117, D16117,  
481 doi:10.1029/2012JD017598, 2012.  
482  
483 Basha, G., and Ratnam, M. V.: Identification of atmospheric boundary layer height over a tropical station using high-  
484 resolution radiosonde refractivity profiles: Comparison with GPS radio occultation measurements, *J. Geophys. Res.*,  
485 114, doi.org/10.1029/2008jd011692, 2009.  
486  
487 Beyerle, G., Gorbunov, M. E., and Ao, C.O.: Simulation studies of GPS radio occultation measurements, *Radio Sci.*,  
488 38, 1084, doi:10.1029/2002RS002800, 2003.  
489  
490 Bretherton, C.S., and Coauthors: Cloud, Aerosol, and Boundary Layer Structure across the Northeast Pacific  
491 Stratocumulus–Cumulus Transition as Observed during CSET, *Mon. Wea. Rev.*, 147, 2083–2102. DOI:  
492 10.1175/MWR-D-18-0281, 2019  
493  
494 Eshleman, V.R.: The radio occultation method for the study of planetary atmospheres, *Planet. Space Sci.*, 21, 1521-  
495 1531, doi.org/10.1016/0032-0633(73)90059-7, 1973.  
496  
497 Feng, X., Xie, F., Ao, C.O., and Anthes, R.A.: Ducting and Biases of GPS Radio Occultation Bending Angle and  
498 Refractivity in the Moist Lower Troposphere, *J. Atmos. Oceanic Technol.*, 37, 1013–1025, doi.org/10.1175/JTECH-  
499 D-19-0206.1, 2020.  
500  
501 Fjeldbo, G., and Eshleman, V.R.: The Atmosphere of Mars Analyzed by Integral Inversion of the Mariner IV  
502 Occultation Data, *Planet. Space Sci.*, 16, 1035-1059, doi.org/10.1016/0032-0633(68)90020-2, 1968.  
503

504 Fjeldbo, G., Kliore, A.J., and Eshleman, V.R.: The Neutral Atmosphere of Venus as Studied with the Mariner V Radio  
505 Occultation Experiment, *Astron. J.*, 76, 123-140, doi.org/10.1086/111096, 1971.

506

507 Garratt, J. R.: Review: the atmospheric boundary layer, *Earth-Sci. Rev.*, 37, 89–134, 1994

508

509 Guo, P., Kuo, Y. H., Sokolovskiy, S. V., and Lenschow, D. H.: Estimating Atmospheric Boundary Layer Depth Using  
510 COSMIC Radio Occultation Data, *J. Atmos. Sci.*, 68, 1703–1713, doi.org/10.1175/2011jas3612.1, 2011.

511

512 Gorbunov, M. E.: Canonical transform method for processing radio occultation data in the lower troposphere, *Radio*  
513 *Sci.*, 37(5), 1076, doi:10.1029/2000RS002592, 2002.

514

515 Gorbunov, M. E., Benzon, H. H., Jensen, A.S, Lohmann, M.S., and Nielsen, A.S.: Comparative analysis of radio  
516 occultation processing approaches based on Fourier integral operators. *Radio Sci.*, 39, RS6004,  
517 <https://doi.org/10.1029/2003RS002916>, 2004

518

519 Healy, S. B.: Radio occultation bending angle and impact parameter errors caused by horizontal refractive index  
520 gradients in the troposphere: A simulation study, *J. Geophys. Res.*, 106, D11, 11875–11889,  
521 doi:10.1029/2001JD900050, 2001.

522

523 Hersbach, H., Bell, B., Berrisford, P., Hirahara, S., Horányi, A., Muñoz-Sabater, J., Nicolas, J., Peubey, C., Radu, R.,  
524 Schepers, D., Simmons, A., Soci, C., Abdalla, S., Abellan, X., Balsamo, G., Bechtold, P., Biavati, G., Bidlot, J.,  
525 Bonavita, M., De Chiara, G., Dahlgren, P., Dee, D., Diamantakis, M., Dragani, R., Flemming, J., Forbes, R., Fuentes,  
526 M., Geer, A., Haimberger, L., Healy, S., Hogan, R. J., Hólm, E., Janisková, M., Keeley, S.,  
527 Laloyaux, P., Lopez, P., Lupu, C., Radnoti, G., de Rosnay, P., Rozum, I., Vamborg, F., Villaume, S., and Thépaut, J.-  
528 N.: The ERA5 Global Reanalysis, *Q. J. Roy. Meteor. Soc.*, 146, 1999–2049, <https://doi.org/10.1002/qj.3803>, 2020.

529

530 Ho, S.-P., Peng, L., Anthes, R. A., Kuo, Y.-H., and Lin, H.-C.: Marine boundary layer heights and their longitudinal,  
531 diurnal and inter-seasonal variability in the southeast Pacific using COSMIC, CALIOP, and radiosonde data. *J.*  
532 *Climate*, 28, 2856–2872, <https://doi.org/10.1175/JCLI-D-14-00238.1>, 2015.

533

534 Jensen, A. S., Lohmann, M.S., Nielsen, A.S. and Benzon, H.-H.: Geometrical optics phase matching of radio  
535 occultation signals, *Radio Sci.*, 39, RS3009, doi:10.1029/2003RS002899, 2004.

536

537 Jensen, A. S., Lohmann, M.S., Benzon, H.-H, and Nielsen, A.S.: Full spectrum inversion of radio occultation signals,  
538 *Radio Sci.*, 38(3), 1040, doi:10.1029/2002RS002763, 2003.

539

540 Johnston, B. R., Xie, F., and Liu, C.: The effects of deep convection on regional temperature structure in the tropical  
541 upper troposphere and lower stratosphere, *J. Geophys. Res.: Atmos.*, 123, 1585–1603,  
542 doi.org/10.1002/2017JD027120, 2018.

543

544 Klein, S. A., and Hartmann, D. L.: The seasonal cycle of low stratiform clouds. *Journal of Climate*, 6, 1587–1606,  
545 doi:10.1175/1520-0442(1993)006<1587:TSCOLS>2.0.CO;2, 1993.

546

547 Kursinski, E. R., Hajj, G. A., Schofield, J. T., Linfield, R. P., and Hardy, K. R.: Observing Earth’s atmosphere with  
548 radio occultation measurements using the Global Positioning System, *J. Geophys. Res.: Atmos.*, 102, 23429–23465,  
549 doi.org/10.1029/97jd01569, 1997.

550

551 Kursinski, E. R., G. A. Hajj, Leroy, S. S., and Herman, B.: The GPS Radio Occultation Technique. *Terr. Atmos.*  
552 *Ocean. Sci. (TAO)*, 11, 53–114, 2000.

553

554 Lewis, E. R.: Marine ARM GPCI Investigation of Clouds (MAGIC) Field Campaign Report. U.S. Department of  
555 Energy, <https://doi.org/10.2172/1343577>, 2016.

556

557 Maddy, E. S. and Barnet, C. D.: Vertical resolution estimates in version 5 of AIRS operational retrievals. *IEEE*  
558 *Transactions on Geoscience and Remote Sensing*, 46, 2375–2384, doi:10.1109/TGRS.2008.917498, 2008.

559

560 Nelson, K. J., Xie, F., Ao, C. O., and Oyola-Merced, M. I.: Diurnal Variation of the Planetary Boundary Layer Height  
561 Observed from GNSS Radio Occultation and Radiosonde Soundings over the Southern Great Plains. *J. Atmos.*  
562 *Oceanic Tech.*, 38, 2081–2093, <https://doi.org/10.1175/jtech-d-20-0196.1>, 2021.

563

564 Nelson, K. J., Xie, F., Chan, B. C., Goel, A., Kosh, J., Reid, T. G. R., Snyder, C. R., and Tarantino, P. M.: GNSS  
565 Radio Occultation Soundings from Commercial Off-the-Shelf Receivers Onboard Balloon Platforms, *Atmos. Meas.*  
566 *Tech.*, <https://doi.org/10.5194/amt-2022-198>, 2022.

567

568 Painemal, D., Minnis, P., and Nordeen, M.: Aerosol variability, synoptic-scale processes, and their link to the cloud  
569 microphysics over the northeast Pacific during MAGIC, *J. Geophys. Res. Atmos.*, 120, 5122–5139,  
570 doi:10.1002/2015JD023175, 2015.

571

572 Patterson, W. L.: Climatology of Marine Atmospheric Refractive Effects: A Compendium of the Integrated Refractive  
573 Effects Prediction System (IREPS) Historical Summaries. Naval Ocean Systems Center,  
574 <https://apps.dtic.mil/sti/pdfs/ADA155241.pdf>, 1982.

575

576 Ramanathan, V., Cess, R. D., Harrison, E. F., Minnis, P., Barkstrom, B. R., Ahmad, E., and Hartmann, D.: Cloud-  
577 radiative forcing and climate: Results from the Earth Radiation Budget Experiment, *Science*, 243, 57–63,  
578 DOI:10.1126/science.243.4887.57, 1989.

579

580 Riehl, H.: *Climate and weather in the tropics*. London: Academic Press. 611 pp. ISBN 0.12.588180.0

581

582 Rocken, C., Anthes, R., Exner, M., Hunt, D., Sokolovskiy, S., Ware, R., Gorbunov, M., Schreiner, W., Feng  
583 D., Herman B., Kuo, Y.-H., Zou, X.: Analysis and validation of GPS/MET data in the neutral atmosphere. *J. Geophys.*  
584 *Res.*, 102, 29849–29866, <https://doi.org/10.1029/97JD02400>, 1997.

585

586 Schreiner, W. S., Weiss, J.P., Anthes, R.A., Braun, J., Chu, V., Fong, J., Hunt, D., Kuo, Y.-H., Meehan, T., Serafino,  
587 W., Sjoberg, J., Sokolovskiy, C., Talaat, E., Wee, T.K., Zeng, Z.: COSMIC-2 Radio Occultation Constellation: First  
588 Results. *Geophys. Res. Lett.*, 47, <https://doi.org/10.1029/2019gl086841>, 2020.

589

590 Seidel, D. J., Ao, C.O. and Li, K.: Estimating climatological planetary boundary layer heights from radiosonde  
591 observations: Comparison of methods and uncertainty analysis, *J. Geophys. Res.*, 115, D16114,  
592 doi:10.1029/2009JD013680, 2010.

593

594 Smith, E. K. and Weintraub, S.: The Constants in the Equation for Atmospheric Refractivity Index at Radio  
595 Frequencies. *Proc. IRE*, 41, 1035–1037, doi:10.1109/JRPROC.1953.274297, 1953.

596

597 Sokolovskiy, S. V.: Modeling and Inverting Radio Occultation Signals in the Moist Troposphere. *Radio Sci.*, 36,  
598 441–458, <https://doi.org/10.1029/1999RS002273>, 2001.

599

600 Sokolovskiy, S. V.: Effect of super refraction on inversions of radio occultation signals in the lower troposphere.  
601 *Radio Sci.*, 38 (3), <https://doi.org/10.1029/2002RS002728>, 2003.

602

603 Sokolovskiy, S. V., Kuo, Y.-H., Rocken, C., Schreiner, W. S., Hunt, D. and Anthes, R. A., 2006: Monitoring the  
604 atmospheric boundary layer by GPS radio occultation signals recorded in the open-loop mode. *Geophys. Res. Lett.*,  
605 33, L12813, doi:10.1029/2006GL025955, 2006.

606

607 Stull, R., Santoso, E., Berg, L. K., and Hacker, J.: Boundary Layer Experiment 1996 (BLX96), *BAMS*, 78,  
608 1149–1158, doi: 10.1175/1520-0477(1997)078<1149:BLEB>2.0.CO;2, 1997.

609

610 Stull, R. B.: *An Introduction to Boundary Layer Meteorology*. Kluwer Academic Publishers, 666 pp., ISBN 90-277-  
611 2768-6, 1988.

612

613 von Engel, A. and Teixeira, J.: A Planetary Boundary Layer Height Climatology Derived from ECMWF Reanalysis  
614 Data, *J. Climate*, 26, 6575–6590, <https://doi.org/10.1175/jcli-d-12-00385.1>, 2013.

615

616 Winning, T. E., Chen, Y.-L., and Xie, F.: Estimation of the marine boundary layer height over the central North Pacific  
617 using GPS radio occultation, *Atmospheric Research*, 183, 362–370, <https://doi.org/10.1016/j.atmosres.2016.08.005>,  
618 2017.

619

620 Wood, R., Mechoso, C. R., Bretherton, C. S., Weller, R. A., Huebert, B., Straneo, F., Albrecht, B. A., Coe, H., Allen,  
621 G., Vaughan, G., Daum, P., Fairall, C., Chand, D., Gallardo Klenner, L., Garreaud, R., Grados, C., Covert, D. S.,  
622 Bates, T. S., Krejci, R., Russell, L. M., de Szoeke, S., Brewer, A., Yuter, S. E., Springston, S. R., Chaigneau, A.,  
623 Toniazzi, T., Minnis, P., Palikonda, R., Abel, S. J., Brown, W. O. J., Williams, S., Fochesatto, J., Brioude, J., and  
624 Bower, K. N.: The VAMOS Ocean-Cloud-Atmosphere-Land Study Regional Experiment (VOCALS-REx): goals,  
625 platforms, and field operations, *Atmos. Chem. Phys.*, 11, 627–654, <https://doi.org/10.5194/acp-11-627-2011>, 2011.

626

627 Xie, F., Syndergaard, S., Kursinski, E. R., and Herman, B.M.: An Approach for Retrieving Marine Boundary Layer  
628 Refractivity from GPS Occultation Data in the Presence of Super-refraction. *J. Atmos. Oceanic Technol.*, 23,  
629 1629–1644, <https://doi.org/10.1175/JTECH1996.1>, 2006.

630

631 Xie, F., Haase, J. S., and Syndergaard, S.: Profiling the Atmosphere Using the Airborne GPS Radio Occultation  
632 Technique: A Sensitivity Study. *IEEE Transactions on Geoscience and Remote Sensing*, 46, 3424–3435,  
633 <https://doi.org/10.1109/tgrs.2008.2004713>, 2008.

634

635 Xie, F., Wu, D. L., Ao, C. O., Kursinski, E. R., Mannucci, A. J., and Syndergaard, S.: Super-refraction effects on GPS  
636 radio occultation refractivity in marine boundary layers, *Geophys. Res. Lett.*, 37,  
637 <https://doi.org/10.1029/2010gl043299>, 2010.

638

639 Xie, F., Wu, D. L., Ao, C. O., Mannucci, A. J., and Kursinski, E. R.: Advances and limitations of atmospheric boundary  
640 layer observations with GPS occultation over southeast Pacific Ocean, *Atmos. Chem. Phys.*, 12, 903–918,  
641 [doi:10.5194/acp-12-903-2012](https://doi.org/10.5194/acp-12-903-2012), 2012.

642

643 Zhou, X., Kollias, P., and Lewis, E.: Clouds, precipitation and marine boundary layer structure during MAGIC. *J.*  
644 *Climate*, 28, 2420–2442, <https://doi.org/10.1175/JCLI-D-14-00320.1>, 2015.